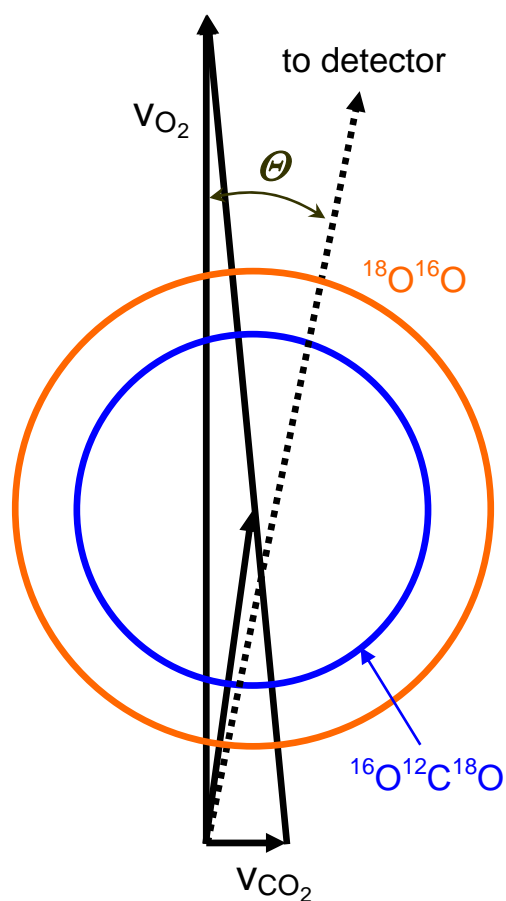
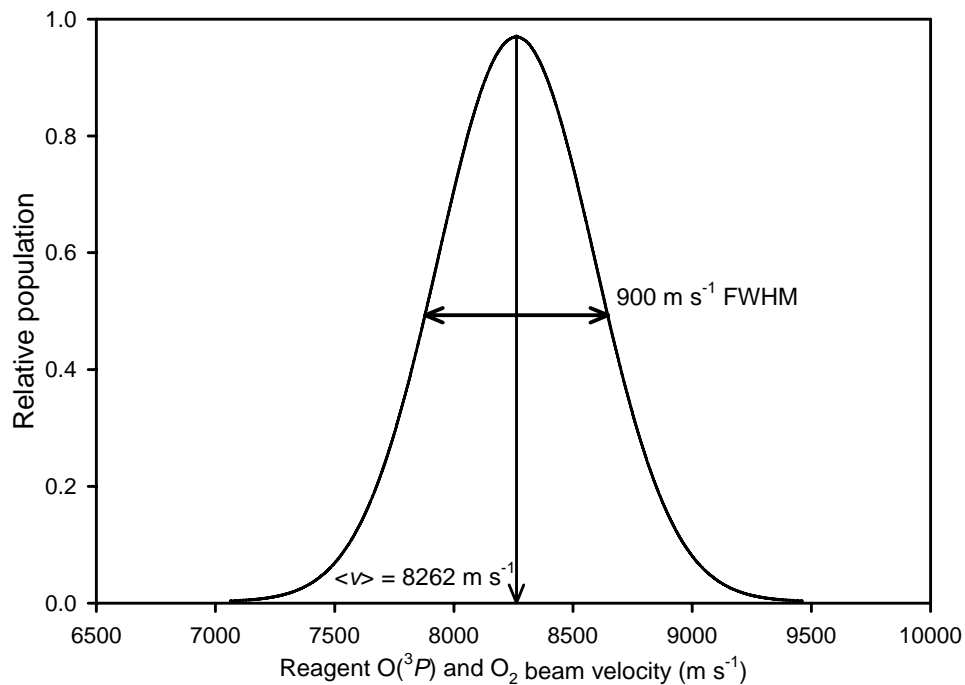


**Supporting Information**  
**for**  
***Hyperthermal O-Atom Exchange Reaction  $O_2 + CO_2$***   
***through a  $CO_4$  Intermediate***

Laurence Y. Yeung, Mitchio Okumura, Jeffrey T. Paci, George C. Schatz, Jianming Zhang, and  
Timothy K. Minton



**Supplemental Figure 1.** Newton diagram for the  $^{16}\text{O}_2 + ^{12}\text{C}^{18}\text{O}_2$  isotope exchange reaction, where  $\langle E_T \rangle = 16\% E_{\text{avail}}$ .  $^{16}\text{O}^{12}\text{C}^{18}\text{O}$  products were peaked near  $\Theta = 6^\circ$  (the smallest angle at which data were collected), indicating that they were scattered mainly in the forward direction with respect to the initial  $^{16}\text{O}_2$  beam. The circles show the locus of velocities for  $^{18}\text{O}^{16}\text{O}$  and  $^{16}\text{O}^{12}\text{C}^{18}\text{O}$  products if the average center-of-mass translational energy is  $\langle E_T \rangle = 16\% E_{\text{avail}}$ .



**Supplemental Figure 2.** Laboratory-frame velocity distribution for the hyperthermal oxygen beam, obtained from TOF distributions of the  $^{16}\text{O}(^3\text{P})$  and  $^{16}\text{O}_2$  beams.

## $P(E_T)$ and $T(\theta_{c.m.})$ of $^{16}\text{O}^{12}\text{C}^{18}\text{O}$ products

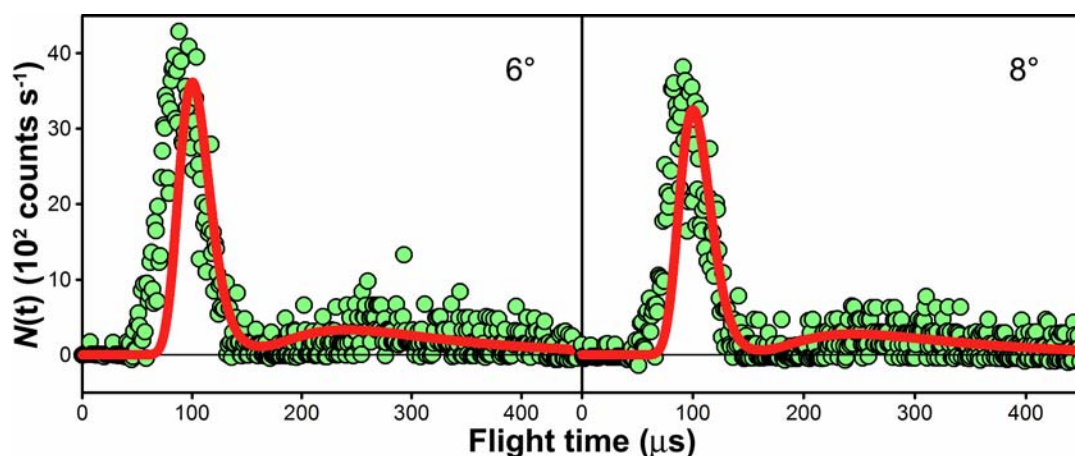
A distribution of available energies can be calculated from the distribution of initial velocities.  $^{12}\text{C}^{18}\text{O}_2$  was estimated to have a laboratory velocity of  $800 \pm 80 \text{ m s}^{-1}$  (*cf.* main text Ref. 4). Given the broad velocity distribution in the  $\text{O}(^3\text{P})/\text{O}_2$  beam ( $8262 \text{ m s}^{-1}$  with  $900 \text{ m s}^{-1}$  FWHM), the velocity spread in the  $^{12}\text{C}^{18}\text{O}_2$  beam was insignificant by comparison, so the hyperthermal oxygen beam largely determined the broad distribution of collision energies sampled in these experiments. The width of the collision energy distribution ( $E_{\text{coll, peak}}$  and FWHM) was calculated by fitting the c.m.  $E_{\text{coll}}$  distribution to a Gaussian form. To calculate the maximum available translational energy in the laboratory frame for  $^{16}\text{O}(^3\text{P}) + ^{12}\text{C}^{18}\text{O}_2$  and  $^{16}\text{O}_2 + ^{12}\text{C}^{18}\text{O}_2$  isotope exchange reactions, an initial  $^{16}\text{O}(^3\text{P})/^{16}\text{O}_2$  beam velocity of  $8862 \text{ m s}^{-1}$  was used because  $< 5\%$  of the  $\text{O}(^3\text{P})/\text{O}_2$  beam had a greater velocity. A non-negligible population of  $^{16}\text{O}^{12}\text{C}^{18}\text{O}$  is observed at translational energies above the maximum allowed for  $^{16}\text{O}(^3\text{P}) + ^{12}\text{C}^{18}\text{O}_2$  collisions at small laboratory angles.

Forward-convolution best fits to the TOF distributions that only treat the  $^{16}\text{O}(^3\text{P}) + ^{12}\text{C}^{18}\text{O}_2$  isotope exchange reaction cannot explain the fastest laboratory data at small laboratory angles (e.g.,  $\Theta = 6^\circ$  and  $8^\circ$ ; see Supplemental Figure 3). Increasing  $\langle E_T \rangle$  in the product  $P(E_T)$  shifts the fastest part of the fit towards shorter flight times at all laboratory angles. While this improves the TOF fits at small laboratory angles, it decreases the quality of the TOF fits at larger laboratory angles (see  $\Theta = 36^\circ$  in Supplemental Figure 4). Introducing the  $^{16}\text{O}_2 + ^{12}\text{C}^{18}\text{O}_2$  isotope exchange reaction yields good fits at all laboratory angles. A sizeable fraction of the products assigned to the  $^{16}\text{O}_2 + ^{12}\text{C}^{18}\text{O}_2$  reaction are slow enough that they do not violate conservation of energy; however, assigning them to the  $^{16}\text{O}(^3\text{P}) + ^{12}\text{C}^{18}\text{O}_2$  reaction leads to poor fits. A c.m. velocity flux diagram of  $^{16}\text{O}^{12}\text{C}^{18}\text{O}$  products is shown in Supplemental Figure 5, in which the observed product flux is peaked in the forward direction.

The angular distribution of  $^{16}\text{O}^{12}\text{C}^{18}\text{O}$  products warrants further discussion. As we mention in the main text, we did not have sufficient sensitivity to detect products scattered in the backwards direction; while this uncertainty prevents us from ruling out a forward-backward symmetric angular distribution of products, both the experimental and theoretical results are consistent with the angular distribution being strongly peaked only in the forward direction. First, the TOF fits at small laboratory angles (e.g.,  $\Theta = 6^\circ$  and  $8^\circ$ ; see Supplemental Figure 1 for the corresponding  $\theta_{c.m.}$ ) are sensitive to both the height and the width of the forward-scattered peak at  $\theta_{c.m.} = 0$ . We were unable to measure a TOF distribution corresponding to  $\theta_{c.m.} = 0$  directly due to the orientation of the chopper wheel in our apparatus, but our data are consistent with a marked increase in the number of

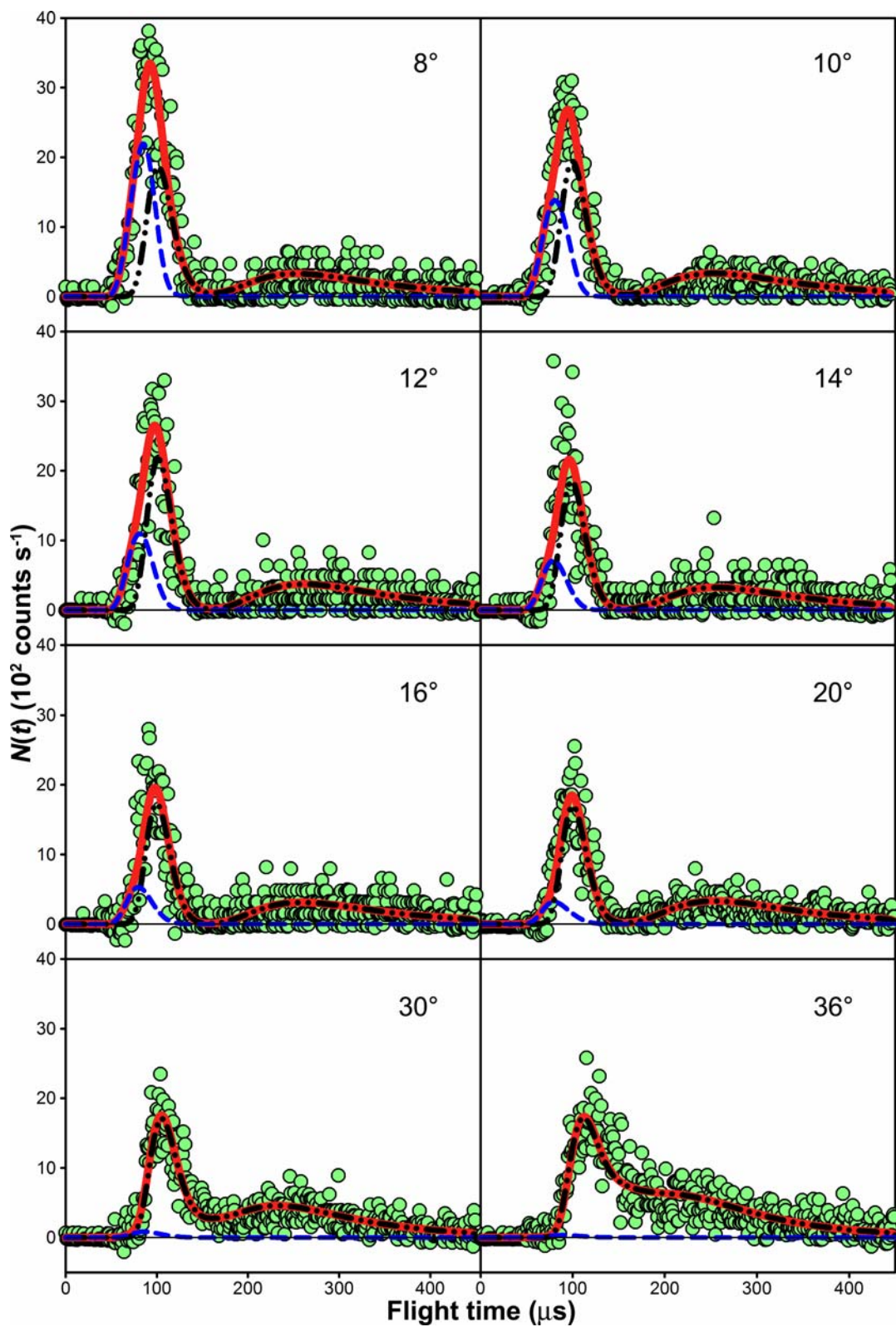
scattered  $^{16}\text{O}^{12}\text{C}^{18}\text{O}$  products at small c.m. angles. Similar forward-scattered angular distributions have been observed for other high-collision-energy isotope exchange experiments with high excess energy performed on our apparatus, e.g.,  $\text{O}(^3\text{P}) + \text{CO}$ , in which the experimental results agreed nearly quantitatively with theoretical calculations.<sup>1</sup> Second, our theoretical calculations predict that the  $\text{CO}_4$  shelf state on the product side should have a high internal energy once  $\text{O}_2$  and  $\text{CO}_2$  surmount the  $45 \text{ kcal mol}^{-1}$  TS3 barrier above  $\text{CO}_4$ . Given the small barrier to  $\text{CO}_4$  dissociation,  $\text{CO}_4$  molecules are unlikely to survive long enough (i.e., for several rotational periods) to yield a forward-backward symmetric angular distribution of products. Third, the overall  $121 \text{ kcal mol}^{-1}$  barrier to  $\text{O}_2 + \text{CO}_2$  isotope exchange implies that small-impact-parameter collisions (“rebounding” reactions) contribute strongly to the observed angular distribution of products, even at the high collision energies probed in this experiment.

Trajectory calculations for this reaction must be performed to test this hypothesis, however. The reaction dynamics could be affected by not only the excess energy in the  $^{16}\text{O}_2$  reagent, but also the distribution of that excess energy, i.e., in the form of vibrations, which were not characterized.  $^{16}\text{O}_2$  has twice the mass of and the same velocity distribution as  $^{16}\text{O}(^3\text{P})$  (see Supplemental Figure 2), so its collisions with  $^{12}\text{C}^{18}\text{O}_2$  have a broader  $E_{\text{coll}}$  distribution. Also, the vibrational temperature of  $^{16}\text{O}_2$  is unknown, so the distribution of total available energy is also wider than that for  $^{16}\text{O}(^3\text{P})$ . Future laboratory work characterizing the  $^{16}\text{O}_2$  portion of the hyperthermal oxygen beam will better constrain this uncertainty.

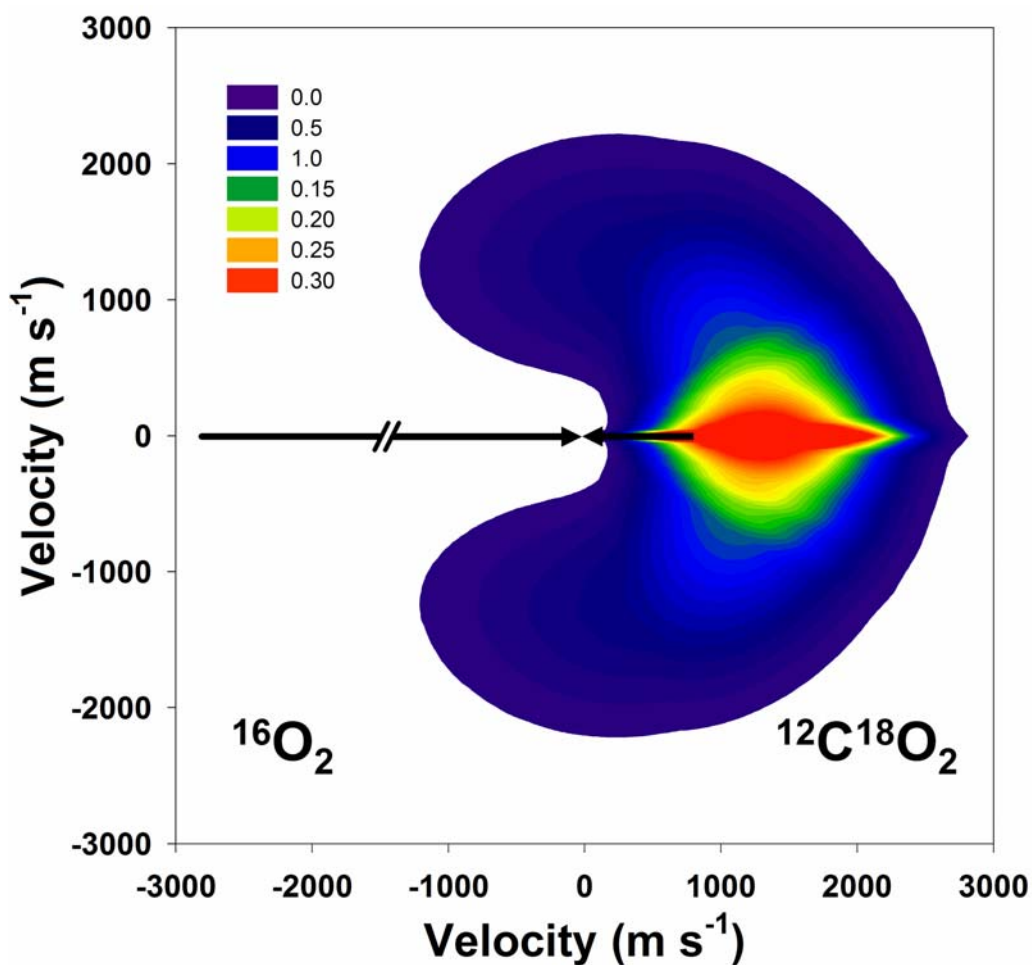


**Supplemental Figure 3.** TOF distributions (green dots) for  $^{16}\text{O}^{12}\text{C}^{18}\text{O}$  products at laboratory angles  $\Theta = 6^\circ$  and  $8^\circ$  with the inelastic scattering signal removed. Also shown are forward-convolution best fits (solid red line) that treat only one isotope exchange reaction,  $^{16}\text{O}(^3\text{P}) + ^{12}\text{C}^{18}\text{O}_2 \rightarrow ^{18}\text{O} + ^{16}\text{O}^{12}\text{C}^{18}\text{O}$ . The forward-convolution fits cannot account for the fastest  $^{16}\text{O}^{12}\text{C}^{18}\text{O}$  product signals at small laboratory angles.

<sup>1</sup> Brunsvold, A. L.; Upadhyaya, H. P.; Zhang, J.; Cooper, R.; Minton, T. K.; Braunstein, M.; Duff, J. W. *J. Phys. Chem. A* **2008**, *112*, 2192-2205.



**Supplemental Figure 4.** TOF distributions for  $^{16}\text{O}^{12}\text{C}^{18}\text{O}$  products ( $m/z = 46$ ) at various laboratory angles  $\Theta$  with the inelastic scattering signal removed. The raw data are shown as circles. Forward-convolution fits of the  $^{16}\text{O}_2 + ^{12}\text{C}^{18}\text{O}_2$  (blue dashed curve) and  $^{16}\text{O}(^3\text{P}) + ^{12}\text{C}^{18}\text{O}_2$  (black dot-dashed curve) channels, along with their sum (red solid curve), are also shown.



**Supplemental Figure 5.** Center-of-mass frame velocity flux contour diagram of  $^{16}\text{O}^{12}\text{C}^{18}\text{O}$  products from  $^{16}\text{O}_2 + ^{12}\text{C}^{18}\text{O}_2$  collisions. Black arrows indicate the initial velocity vectors of each reagent in the c.m. frame. Product flux values increase from blue (low) to red (high).  $^{16}\text{O}^{12}\text{C}^{18}\text{O}$  products are scattered in the forward direction ( $^{16}\text{O}_2$ 's original direction) with a relatively small velocity. Elastic collisions between  $^{16}\text{O}_2$  and  $^{16}\text{O}^{12}\text{C}^{18}\text{O}$  would yield  $^{16}\text{O}^{12}\text{C}^{18}\text{O}$  products with a velocity distribution peaked at  $v = 3435 \text{ m s}^{-1}$ . These data are consistent with a mechanism in which the  $^{16}\text{O}^{12}\text{C}^{18}\text{O}$  products 'rebound' after the  $^{16}\text{O}_2 + ^{12}\text{C}^{18}\text{O}_2$  collision.

## Theoretical methods: Stationary point characterization

Stationary points on the lowest triplet potential energy surface were characterized using the MOLPRO<sup>2</sup> electronic structure code. The properties of one bound and three transition states calculated at the CCSD(T)/aug-cc-pVTZ level of theory are summarized in Supplemental Table 1.

We observed some evidence for multi-reference character in CO<sub>4</sub>. An additional bound state was found 0.8 kcal mol<sup>-1</sup> above the energy of CO<sub>4</sub> at the MP2/cc-pVTZ level of theory, although it does not exist at the CCSD(T)/aug-cc-pVTZ level; the species is believed to be a resonance structure of CO<sub>4</sub>(<sup>3</sup>A''). A spin contamination of  $\langle S^2 - S_z^2 - S_z \rangle = 0.011$  in the region of the PES near TS3 also suggests some multi-reference character. Thus, CASPT2/cc-pVTZ calculations, which represent resonance qualitatively correctly and do not suffer from spin contamination, were performed to validate the CCSD(T) structures and energies. CO<sub>4</sub>(<sup>3</sup>A'') was confirmed as a resonance hybrid of two bound-state structures, although the contribution from the single-reference structure to the resonance hybrid dominates the final geometry. The results of those calculations are summarized in Supplemental Table 2.

A grid-based search revealed that TS3 is bound by 0.02 kcal mol<sup>-1</sup> when zero-point energy is not considered, and that TS3 is connected to CO<sub>4</sub>; a displacement in O<sub>d</sub> < 0.01 Å towards CO<sub>4</sub> produced CO<sub>4</sub> upon geometry optimization. Thus it acts as an 'effective' transition state for CO<sub>4</sub> isomerization.

The uncertainty in the CCSD(T)/aug-cc-pVTZ energies is unknown. However, a similar study in which the stationary points of the closely-related O(<sup>3</sup>P) + CO<sub>2</sub> system were characterized has recently been completed. In addition to CCSD(T)/aug-cc-pVTZ simulations, W4 (close to full configuration interaction and the infinite basis set limit) calculations<sup>3</sup> were also performed, as they were found to be affordable, albeit marginally.<sup>4</sup> The differences between the CCSD(T) and W4 results for the transition and bound states indicated a mean-unsigned error of 2.2 kcal mol<sup>-1</sup>. We expect the errors in the analogous O<sub>2</sub> + CO<sub>2</sub> energies to be approximately the same.

---

<sup>2</sup> Werner, H.-J.; Knowles, P. J.; Lindh, R.; Manby, F. R.; Schutz, M.; Celani, P.; Korona, T.; Rauhut, G.; Amos, R. D.; Bernhardsson, A.; Berning, A.; Cooper, D. L.; Deegan, M. J. O.; Dobbyn, A. J.; Eckert, F.; Hampel, C.; Hetzer, G.; Lloyd, A. W.; McNicholas, S. J.; Meyer, W.; Mura, M. E.; Nicklass, A.; Palmieri, P.; Pitzer, R.; Schumann, U.; Stoll, H.; Stone, A. J.; Tarroni, R.; Thorsteinsson, T. *MOLPRO*, v. 2006.1, a package of *ab initio* programs.

<sup>3</sup> Karton, A.; Rabinovich, E.; Martin, J. M. L.; Ruscic, B. *J. Chem. Phys.* **2006**, *125*, 144108.

<sup>4</sup> Paci, J. T.; Martin, J. M. L.; Schatz, G. C.; Minton, T. K. unpublished.

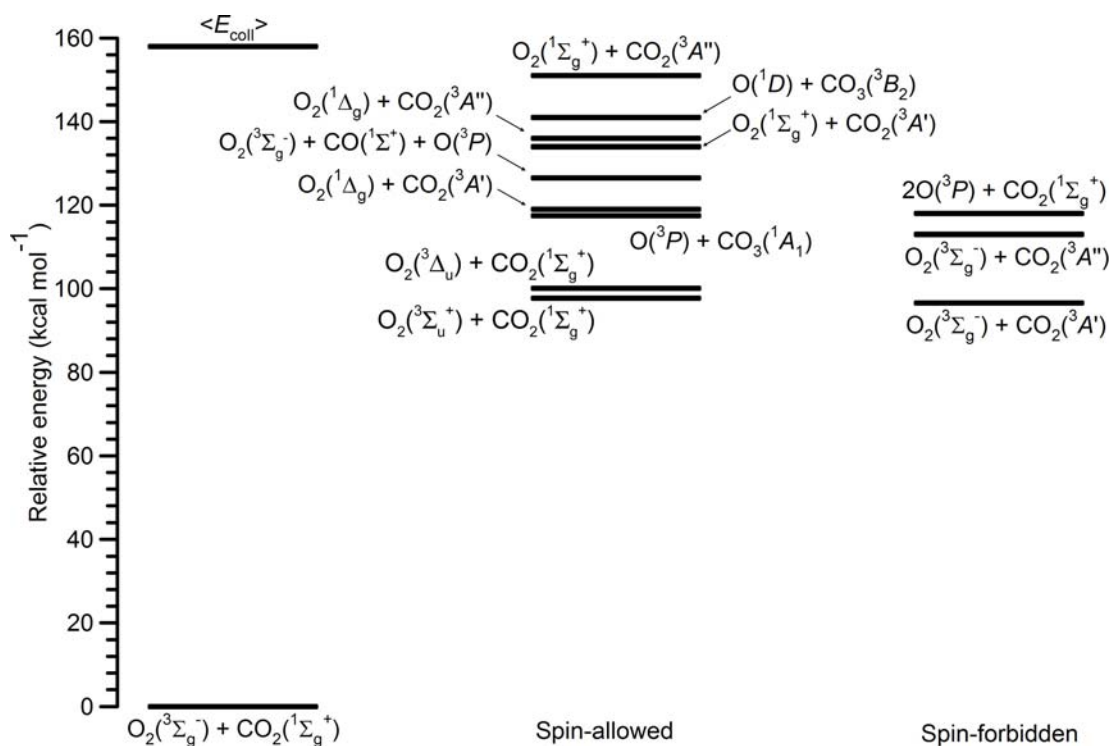
	CO <sub>4</sub>	TS1	TS2	TS3
$\Delta E$	76.0 (76.4)	77.9 (77.9)	80.0 (78.3)	120.9 (121.8)
$r(\text{C-O}_a)$	1.20	1.18	1.25	1.20
$r(\text{C-O}_b)$	1.29	1.27	1.20	1.35
$r(\text{C-O}_c)$	1.40	1.53	1.52	1.35
$r(\text{O}_c\text{-O}_d)$	1.34	1.30	1.30	1.72
$\theta(\text{O}_a\text{-C-O}_b)$	122	135	131	127
$\theta(\text{O}_b\text{-C-O}_c)$	116	105	119	106
$\theta(\text{C-O}_c\text{-O}_d)$	107	98	105	88

**Supplemental Table 1.** Energies and properties of stationary points associated with the exchange reaction  $\text{O}_2 + \text{CO}_2 \rightarrow \text{O}_2 + \text{CO}_2$  on the lowest triplet potential energy surface calculated at the CCSD(T)/aug-cc-pVTZ level of theory. Restricted Hartree-Fock reference wavefunctions were employed. Distances are in angstroms, angles in degrees, and energies in kcal mol<sup>-1</sup>. Zero-point-corrected energies are in parentheses. Refer to Figure 3 in the main text for the atom-labeling scheme. The structures are planar, and have  $C_s$  symmetry except for TS3, which has  $C_{2v}$  symmetry.

	CO <sub>4</sub>	TS1	TS2	TS3
$C_{\text{HF}}$	0.973	0.977	0.969	0.945
$\Delta E$	91.2	95.6	97.1	137.4
$r(\text{C-O}_a)$	1.19	1.17	1.26	1.18
$r(\text{C-O}_b)$	1.32	1.29	1.17	1.37
$r(\text{C-O}_c)$	1.39	1.52	1.62	1.37
$r(\text{O}_c\text{-O}_d)$	1.32	1.29	1.26	1.57
$\theta(\text{O}_a\text{-C-O}_b)$	125	138	139	130
$\theta(\text{O}_b\text{-C-O}_c)$	112	101	120	101
$\theta(\text{C-O}_c\text{-O}_d)$	110	95	106	88

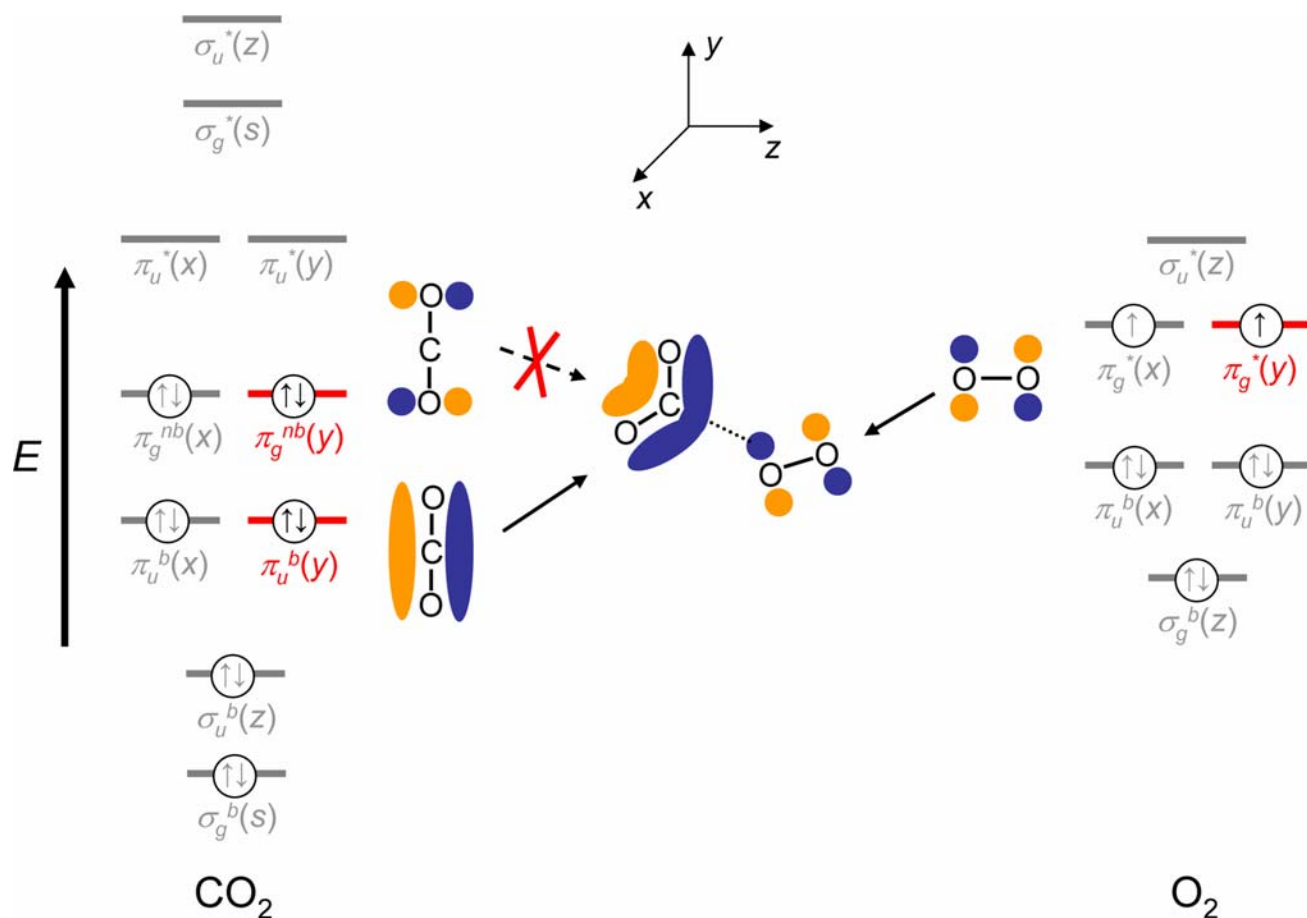
**Supplemental Table 2.** Energies and properties of stationary points associated with the exchange reaction  $\text{O}_2 + \text{CO}_2 \rightarrow \text{O}_2 + \text{CO}_2$  on the lowest triplet potential energy surface calculated at the CASPT2/cc-pVTZ level of theory. No zero-point-corrected energies were calculated at this level of theory.  $C_{\text{HF}}$  values are the coefficients associated with the Hartree-Fock configurations in the [8,10]-CASSCF expansions of the wavefunctions. The atom-labeling scheme and measurement units are the same as in Supplemental Table 1.

## Energetically-allowed product channels

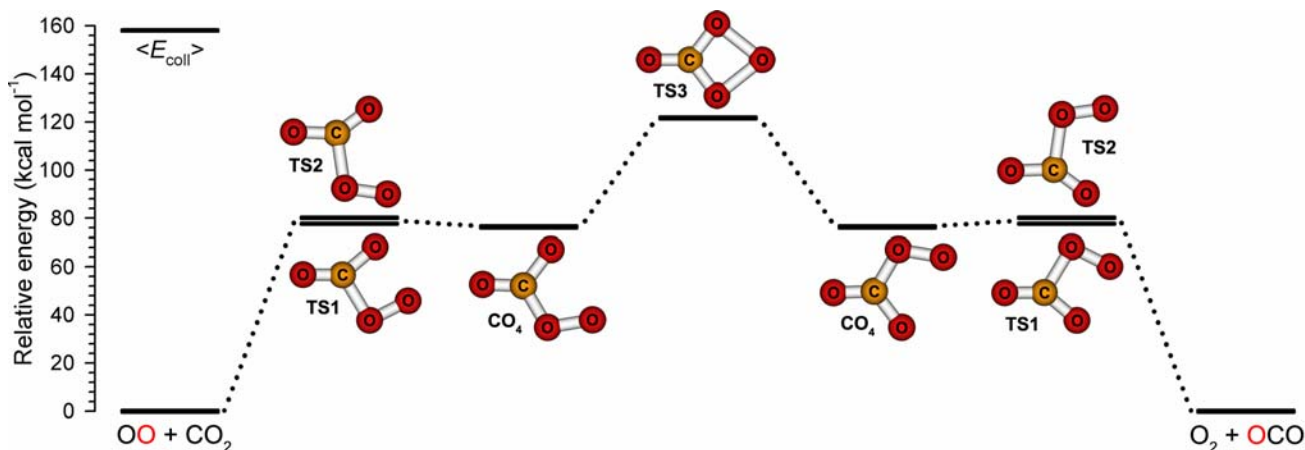


**Supplemental Figure 6.** Energetically-allowed neutral product channels from O<sub>2</sub> + CO<sub>2</sub> collisions. Energies are taken from the NIST Webbook [<http://webbook.nist.gov>], Mebel *et al.* (2004), and Braunstein and Duff (2000). See main text for references.

## Proposed adiabatic reaction mechanism



**Supplemental Figure 7.** Molecular orbital diagrams for  $\text{O}_2$  and  $\text{CO}_2$ , adapted from DeKock and Gray [DeKock, R.L. and Gray, H.B.; *Chemical Structure and Bonding*; Benjamin/Cummings Publishing Company, Inc.: Menlo Park, 1980]. Sketches of the highlighted orbitals are shown. As  $\text{O}_2$  collides with  $\text{CO}_2$ , it becomes stretched. In addition,  $\text{CO}_2$  bends, increasing the energy of its doubly occupied, in-plane  $\pi$ -orbitals,  $\pi_u^b$  and  $\pi_g^{nb}$ . A weak interaction between the  $\pi_g^*$  orbital on  $\text{O}_2$  and the  $\pi_u^b$  orbital on  $\text{CO}_2$  is likely responsible for the small ( $1.5 \text{ kcal mol}^{-1}$ ) binding energy of  $\text{CO}_4$ . The  $\pi_g^{nb}$  orbital does not interact, to first approximation, due to symmetry.



**Supplemental Figure 8.** Energy-level diagram along the proposed  $\text{O}_2 + \text{CO}_2$  reaction path.